

AD-A112 825

HONEYWELL SYSTEMS AND RESEARCH CENTER MINNEAPOLIS MN

F/6 14/2

MONOLITHIC ACCELEROMETER.(U)

DEC 81 H A GUSTAFSON

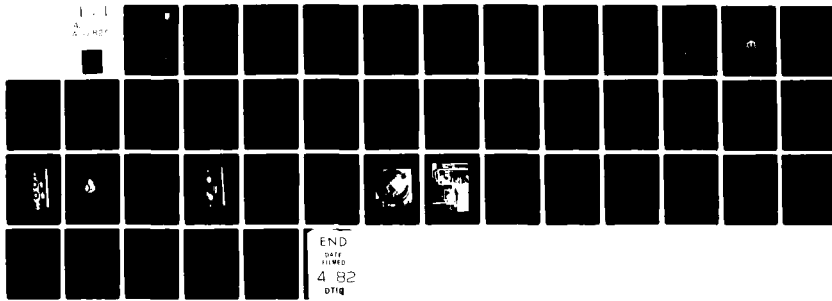
F33615-80-C-1117

UNCLASSIFIED

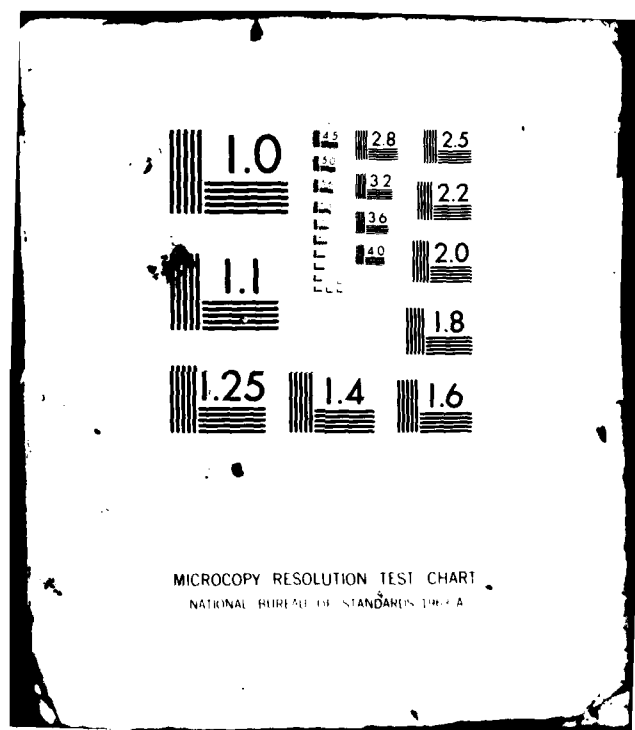
81SRC76

NL

1-1
A-112 825



END
DATE
FILMED
4 82
DTIC



AD A 112825

AFWAL-TR-81-1242



MONOLITHIC ACCELEROMETER

Harry A. Gustafson
Honeywell Systems and Research Center
2600 Ridgway Parkway, PO Box 312
Minneapolis, Minnesota 55440

December 1981

Final Report for Period 6 September 1980 - 31 October 1981

Approved for public release; distribution unlimited.

DTIC
ELECTE
MAR 31 1982
S A D

AVIONICS LABORATORY
AIR FORCE WRIGHT AERONAUTICAL LABORATORIES
AIR FORCE SYSTEMS COMMAND
WRIGHT-PATTERSON AIR FORCE BASE, OHIO 45433

82 03 30 008

DTIC FILE COPY

NOTICE

When Government drawings, specifications, or other data are used for any purpose other than in connection with a definitely related Government procurement operation, the United States Government thereby incurs no responsibility nor any obligation whatsoever; and the fact that the government may have formulated, furnished, or in any way supplied the said drawings, specifications, or other data, is not to be regarded by implication or otherwise as in any manner licensing the holder or any other person or corporation, or conveying any rights or permission to manufacture, use, or sell any patented invention that may in any way be related thereto.

This report has been reviewed by the Office of Public Affairs (ASD/PA) and is releasable to the National Technical Information Service (NTIS). At NTIS, it will be available to the general public, including foreign nations.

This technical report has been reviewed and is approved for publication.

Richard W. Jacobs
PROJECT ENGINEER

Ronald L. Ringo
RONALD L. RINGO, Chief
Reference Systems Branch
System Avionics Division
Avionics Laboratory

FOR THE COMMANDER

Richard H. Boivin
RICHARD H. BOIVIN, Colonel, USAF
Chief, System Avionics Division
Avionics Laboratory

Accession For	
NTIS GRA&I	<input checked="" type="checkbox"/>
DTIC TAB	<input type="checkbox"/>
Unannounced	<input type="checkbox"/>
Justification	
By	
Distribution/	
Availability Codes	
Dist	Avail and/or Special

If your address has changed, if you wish to be removed from our mailing list, or if the addressee is no longer employed by your organization please notify AFSC/PMREB, W-PAFB, OH 45433 to help us maintain a current mailing list.

Copies of this report should not be returned unless return is required by security considerations, contractual obligations, or notice on a specific document.

UNCLASSIFIED

SECURITY CLASSIFICATION OF THIS PAGE (WHEN DATA ENTERED)

REPORT DOCUMENTATION PAGE		READ INSTRUCTIONS BEFORE COMPLETING FORM
1. REPORT NUMBER AFWAL-TR-81-1242	2. GOV'T ACCESSION NUMBER AD-A112 825	3. RECIPIENT'S CATALOG NUMBER
4. TITLE (AND SUBTITLE) MONOLITHIC ACCELEROMETER	5. TYPE OF REPORT/PERIOD COVERED Final Report 6 September 1980-31 October 1981	
7. AUTHOR(S) Harry A. Gustafson	6. PERFORMING ORG. REPORT NUMBER 81SRC76	
9. PERFORMING ORGANIZATIONS NAME/ADDRESS Honeywell Systems and Research Center 2600 Ridgway Parkway, PO Box 312 Minneapolis, Minnesota 55440	8. CONTRACT OR GRANT NUMBER(S) F33615-80-C-1117	
11. CONTROLLING OFFICE NAME/ADDRESS Air Force Avionics Laboratory Air Force Wright Aeronautical Laboratories Wright-Patterson AFB, Ohio 45433	10. PROGRAM ELEMENT PROJECT, TASK AREA & WORK UNIT NUMBERS 62204F, 6095, 12, 23	
14. MONITORING AGENCY NAME/ADDRESS (IF DIFFERENT FROM CONT. OFF.)	12. REPORT DATE December 1981	
	13. NUMBER OF PAGES 45	
	15. SECURITY CLASSIFICATION (OF THIS REPORT) Unclassified	
16. DISTRIBUTION STATEMENT (OF THIS REPORT) Approved for public release; distribution unlimited.		
17. DISTRIBUTION STATEMENT (OF THE ABSTRACT ENTERED IN BLOCK 20, IF DIFFERENT FROM REPORT)		
18. SUPPLEMENTARY NOTES		
19. KEY WORDS (CONTINUE ON REVERSE SIDE IF NECESSARY AND IDENTIFY BY BLOCK NUMBER) Accelerometer Single-crystal silicon Diaphragm Silicon Monolithic		
20. ABSTRACT (CONTINUE ON REVERSE SIDE IF NECESSARY AND IDENTIFY BY BLOCK NUMBER) An investigation of the monolithic accelerometer was carried out to evaluate its potential for inertial navigation applications. The work included analysis and design studies, construction of a breadboard accelerometer, and laboratory testing. The approach used a suspension of two single-crystal silicon diaphragms joined to a frame of silicon or pyrex. Gold diffusion, thermoelectric, and optical contact bonds were used in the assembly. A differential capacitance pickoff was used to sense acceleration. Digital readout was obtained from the differential output of — 3001		

HD-16 REV 11/74

DD FORM 1473 EDITION OF 1 NOV 55 IS OBSOLETE
1 JAN 73

UNCLASSIFIED

SECURITY CLASSIFICATION OF THIS PAGE (WHEN DATA ENTERED)

UNCLASSIFIED

SECURITY CLASSIFICATION OF THIS PAGE (WHEN DATA ENTERED)

two oscillators, each slaved in frequency to its associated pickoff capacitor. Tests were conducted for bias, scale factor, scale factor linearity, and threshold. The tests showed that performance was limited by milli-g variations in bias and scale factor. The instabilities are attributed to residual stresses in the diaphragm suspension, resulting from the high-temperature bonding process. Recommendations are given for extending the concept to improved performance.

Accession For	
DTIC GARRI	<input checked="" type="checkbox"/>
DTIC TAB	<input type="checkbox"/>
Unannounced	<input type="checkbox"/>
Justification	
By	
Distribution/	
Availability Codes	
Dist	Avail and/or Special
A	



UNCLASSIFIED

SECURITY CLASSIFICATION OF THIS PAGE (WHEN DATA ENTERED)

FOREWORD

This report describes the work performed on the monolithic accelerometer to evaluate its potential for inertial navigation applications. The approach involves the use of single-crystal silicon as the suspension element. Two silicon diaphragms carrying the proof mass are joined to the silicon or pyrex frame of the accelerometer. Bonding of the silicon and pyrex parts is accomplished by gold diffusion, thermoelectric, and optical contact methods. Two versions of the accelerometer were constructed: an integral diaphragm model in which the silicon diaphragm and its adjoining frame are one piece, and a silicon/pyrex model in which the diaphragm is a disc bonded to a pyrex frame.

The acceleration pickoff consists of a capacitor at each end, operating differentially to sense displacement of the diaphragms. Each pickoff capacitor is operated with its own oscillator, producing a frequency proportional to capacitance. Digital output is obtained by generating the difference frequency of the two oscillators in an up-down counter.

Tests were made on bias, scale factor, scale factor linearity, threshold, and reaction time. The results showed milli-g variations in bias and scale factor on a day-to-day basis, as well as in temperature sensitivity. The instabilities are attributed to residual stresses in the diaphragms due to the high temperatures used in the gold diffusion and thermoelectric bonding processes. Ways of achieving improved performance are recommended. These include making lower-temperature bonds, reducing the parts count to three using a single diaphragm, and providing temperature compensation.

TABLE OF CONTENTS

Section		Page
1	INTRODUCTION	1
2	APPROACH	2
3	ANALYSIS AND DESIGN	4
	Diaphragm	4
	Accelerometer Dimensions	8
	Proof Mass	8
	Capacitance Pickoff	10
	Materials Selection	10
	Readout Electronics	11
4	FABRICATION	17
	Integral Diaphragm Model	17
	Silicon/Pyrex Model	21
	Electronics	22
5	TESTING	24
6	RELIABILITY AND MAINTAINABILITY	28
	Gold Diffusion Bond	28
	Optical Contact Bond	28
	Diaphragm Rupture	29
	Mass Attachments	29
	Capacitor Electrode on End Disc	29
	Capacitor Electrode on Silicon Diaphragm	29

PRECEDING PAGE BLANK NOT REPRODUCED

TABLE OF CONTENTS (concluded)

Section		Page
	Wiring Connections to Capacitor Electrodes	30
	Voltage Breakdown Across Capacitor	30
	Failure Estimation	30
7	RECOMMENDATIONS FOR FUTURE WORK	33
	Low-Temperature Bonding	33
	All-Silicon End Discs	33
	Single-Diaphragm Suspension	34
	Temperature Compensation	35
8	CONCLUSIONS	36
REFERENCES		37

LIST OF ILLUSTRATIONS

Figure		Page
1	Monolithic Accelerometer: Integral Diaphragm Model	2
2	Monolithic Accelerometer: Silicon/Pyrex Model	3
3	Deflection of Diaphragm Under Load W	4
4	Accelerometer Deflection Per g: Integral Diaphragm Model	6
5	Stress at Inner Radius of Diaphragm: Integral Diaphragm Model	7
6	Accelerometer Deflection Per g: Silicon/Pyrex Model	9
7	Stress at Inner Radius of Diaphragm: Silicon/Pyrex Model	9
8	Readout Electronics	12
9	Oscillating Voltage Across C_x	14
10	Piece Parts for Integral Diaphragm Model	19
11	Assembled Integral Diaphragm Accelerometer	20
12	Piece Parts for Silicon/Pyrex Model	22
13	Accelerometer Test Fixture on Dividing Head (Readout electronics and accelerometer in place.)	25
14	Test Setup Showing Dividing Head, Temperature Chamber, and Data Recording Rack	26
15	Single-Diaphragm Accelerometer (Only three parts and two bonds are required.)	34

SECTION 1

INTRODUCTION

As inertial navigation technology continues to progress, there is a need to develop low-cost accelerometers of navigation system grade. These applications include the need for small size, low cost, no thermal control, high reliability, easy maintenance, and rapid reaction time.

The objective of this study was to assess the feasibility of the monolithic accelerometer concept for these applications. The work involved analysis and design studies, construction of a breadboard accelerometer, and laboratory testing to evaluate its potential for navigation system applications.

As a baseline for concept evaluation, the following performance goals were established for the accelerometer:

Bias stability	100/ μ g
Bias temperature sensitivity	1 μ g/ $^{\circ}$ C
Scale factor linearity	0.001%
Scale factor stability	100 ppm
Scale factor temperature sensitivity	1 ppm/ $^{\circ}$ C
Scale factor symmetry	2 μ g/g
Dynamic range	\pm 10g
Reaction time	1 minute
Threshold	50 μ g

This report discusses the results of the effort in the categories of analysis and design, fabrication, testing, reliability and maintainability, and recommendations for further work.

SECTION 2

APPROACH

In this concept, the approach is to use single-crystal silicon for the accelerometer suspension because of its low creep and superior stability. Also, it is desired to incorporate the suspension in a monolithic frame, preferably of the same material. The configuration chosen is shown in Figure 1.

The suspension consists of two silicon diaphragms, supporting a proof mass as shown. In the figure the diaphragm, cylindrical frame, and center post are an integral unit, made from one piece of silicon. The end caps constitute part of the frame and support one plate of the capacitance pickoff. In the presence of acceleration, the pickoff capacitors change differentially to produce an acceleration original.

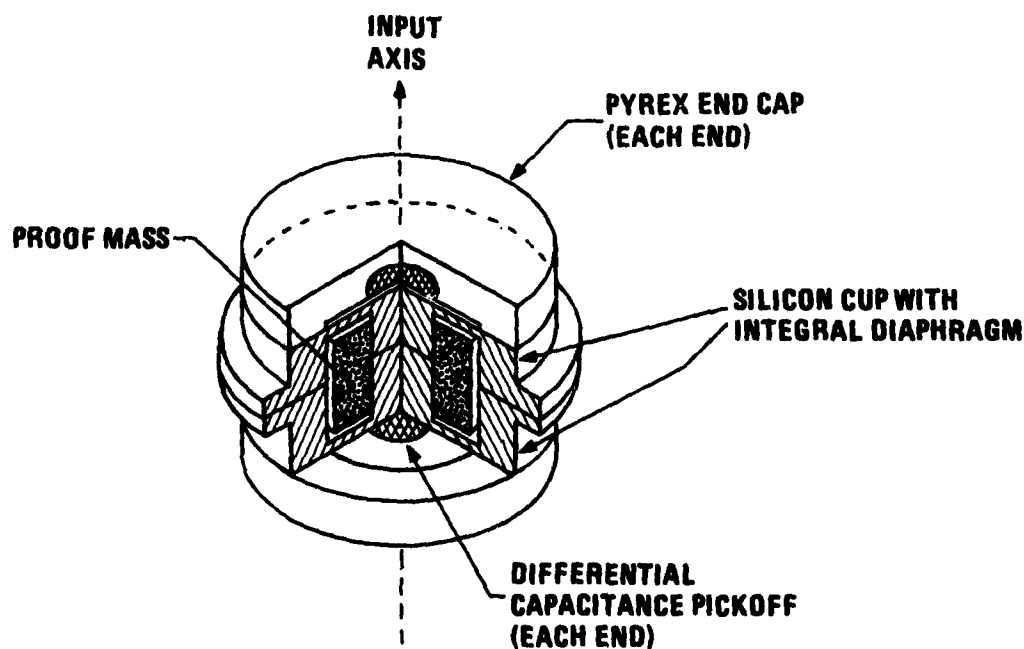


Figure 1. Monolithic Accelerometer: Integral Diaphragm Model

Digital readout is provided by means of two oscillators, each associated with its pickoff capacitor. Each oscillator frequency is proportional to capacitance, and is measured differentially in an up-down counter to generate a digital output of acceleration.

Two models were built. The second model, very similar to the first, is shown in Figure 2. It differs primarily in the assembly bonding methods, using a cylinder pyrex body as shown. The pickoff arrangement and readout method are the same for both models.

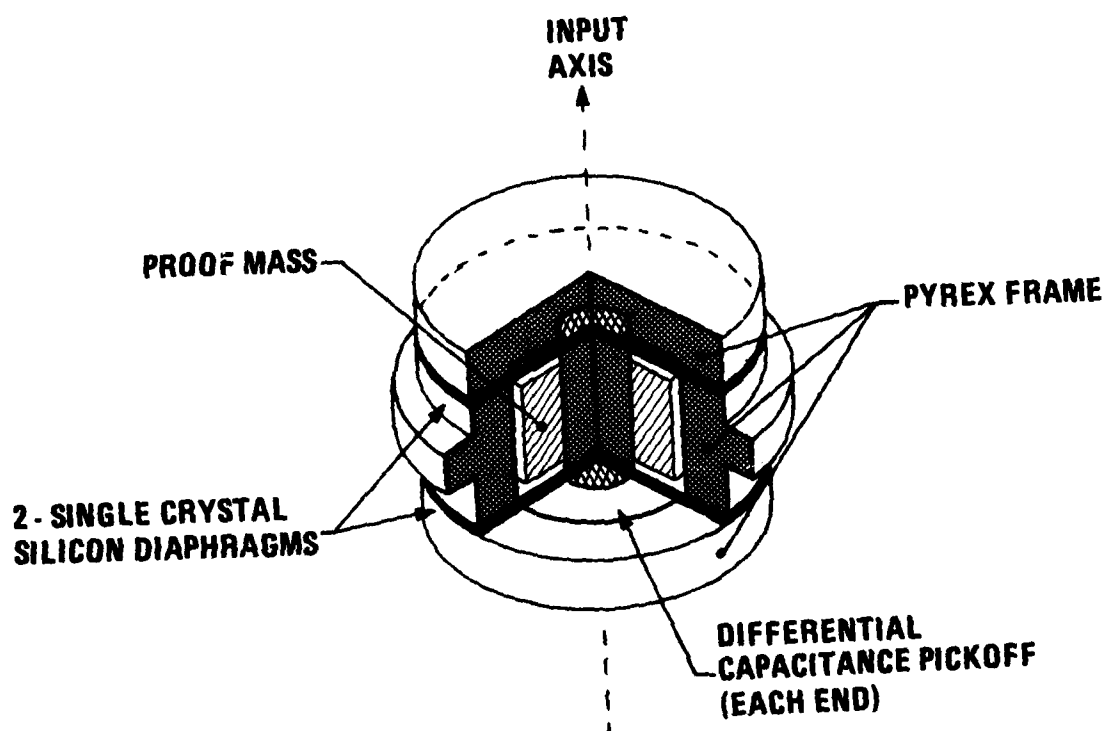


Figure 2. Monolithic Accelerometer: Silicon/Pyrex Model

SECTION 3

ANALYSIS AND DESIGN

The analysis and design effort was directed toward defining a specific configuration of the accelerometer. This work included scaling and dimensioning the diaphragm suspension and proof mass, designing the accelerometer body, and designing the capacitance pickoff and the readout electronics. These topics are discussed below.

DIAPHRAGM

To define the diaphragm suspension requires working with the geometry parameters of the inner radius, outer radius, and thickness. For purposes of modeling deflection, a diaphragm with imbedded supports at the inner and outer edges is considered, as shown in Figure 3. Then the deflection per g of the diaphragm, and also the stress at the

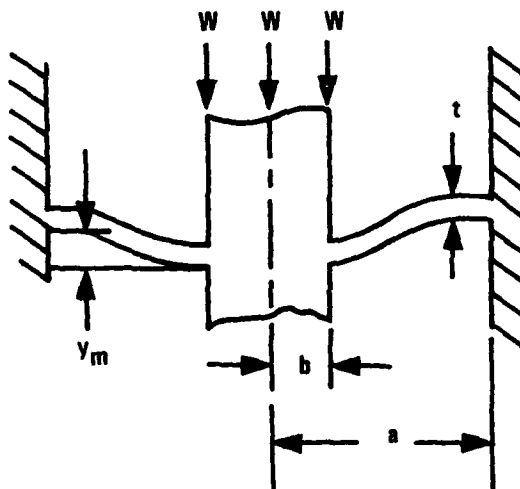


Figure 3. Deflection of Diaphragm Under Load W

inner and outer edges, are examined. Since the outer edge is supported over a longer circumference than the inner edge, the inner edge will show the larger stress.

The deflection, y , as a function of the inertial force W , is given by¹

$$y = \frac{3W (1 - \nu^2) a^2}{4\pi E t^3} \left[1 - \left(\frac{b}{a} \right)^2 - \frac{4b^2}{a^2 - b^2} \left(\ln \frac{a}{b} \right)^2 \right]$$

where a , b , and t are geometrical dimensions of the structure, and E and ν are modulus of elasticity (Young's modulus) and Poisson's ratio of the material of diaphragm, respectively.

For silicon, $E = 1.33 \times 10^{10}$ kg/m² (18.94×10^6 psi) and $\nu = 0.242$ are chosen. For the mass, $W = 9.34$ grams (0.206 lb) is chosen, corresponding to the mass actually used in the integral silicon diaphragm model. Then the deflection per g is calculated for a range of diaphragm radii. As a starting point, the inner radius is fixed at 0.64 cm (0.25 in.) and the outer radius is varied for a range of diaphragm thicknesses. The resulting calculated deflections are shown in Figure 4. In this figure it can be seen that the deflections range from 0.025 μ m to 0.1 μ m (1 to 4 μ in.). For a given deflection, the corresponding resonant frequency can be assigned as shown. The diaphragm thicknesses of 0.30 mm to 0.41 mm (0.012 in. to 0.016 in.) are representative of achievable thickness in the fabrication process.

For purposes of comparison, the dimensions selected for the integral diaphragm model (inner and outer radii), and the attained deflection per g (based on capacitance measurements), are plotted as the small

¹R.J. Roark, Formulas for Stress and Strain, Second Edition. New York: McGraw-Hill, 1943, Chapter 10.

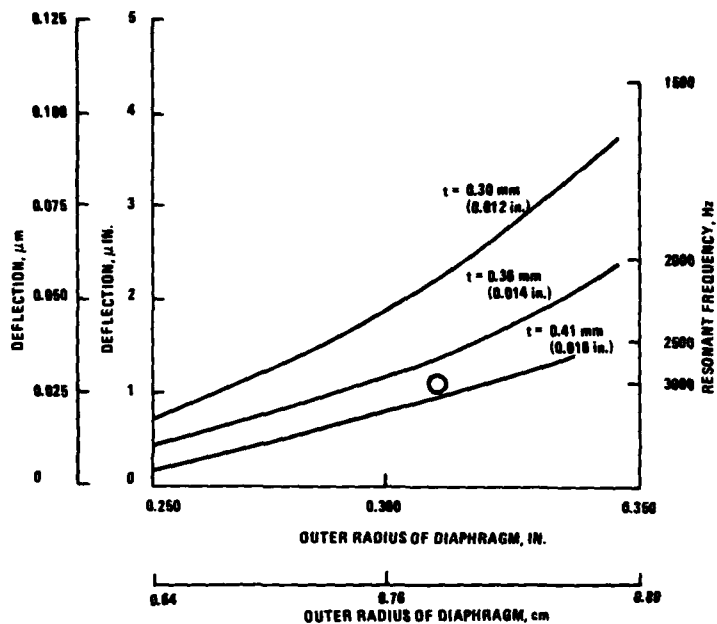


Figure 4. Accelerometer Deflection Per g: Integral Diaphragm Model

circle in Figure 4. The location of the circle in the family of diaphragm thicknesses indicates that a thickness of 0.4 mm (0.016 in.) will produce the observed deflection. This agrees closely with the measured thickness for this model. Once the inner and outer radii are fixed, changing thickness is the most convenient way to change the deflection per g.

For increased sensitivity, a large deflection is desired, but this is gained only at a lowering of the resonant frequency. It is well to keep the resonant frequency above 1500 Hz. Although the navigational needs are quite well met over the range of 0 to 100 Hz, a wider signal pass-band up to several hundred hertz is required.

At the same time that the parameters affecting deflection are varied, consideration must also be given to stress in the diaphragm. For an imbedded diaphragm the stress is given by¹

$$S_{in} = \frac{3W}{2\pi t^2} \left[1 - \frac{2a^2}{a^2 - b^2} \ln \frac{a}{b} \right]$$

and

$$S_{out} = \frac{3W}{2\pi t^2} \left[1 - \frac{2b^2}{a^2 - b^2} \ln \frac{a}{b} \right]$$

where S_{in} and S_{out} are the stresses at the inner and outer edges, respectively. Of the two boundaries, the stresses at the inner edge are the largest. The stress at intermediate points will lie between the values for the two edges.

Using the same values for a , b , and W as before, the calculated stresses for the inner edge are obtained as shown in Figure 5. As an example, if a point is located for the dimensions of inner and outer radii for the silicon model, also corresponding to the thickness represented in Figure 4, it can be seen that the stress is 2.8 kg/cm^2 (40 psi) for a loading of $1g$. For a $10g$ load the stress

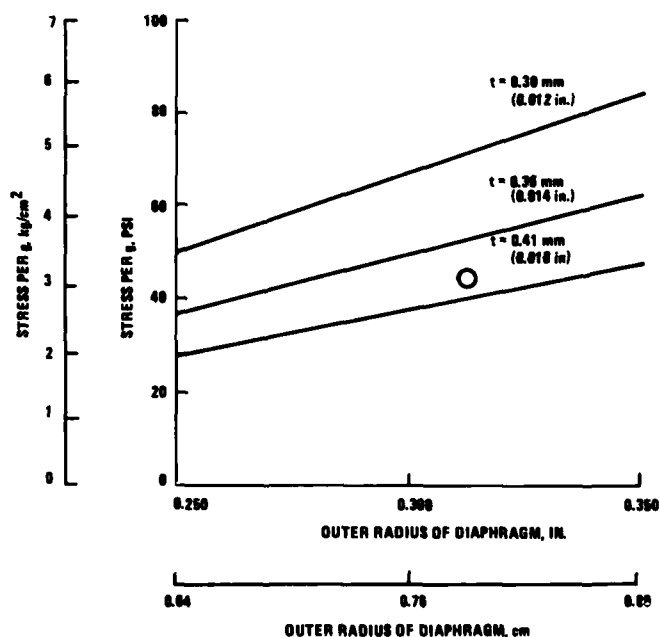


Figure 5. Stress at Inner Radius of Diaphragm: Integral Diaphragm Model

would be 28 kg/cm^2 (400 psi). The modulus of rupture for silicon ranges from 700 to 3500 kg/cm^2 (10,000 to 50,000 psi), depending on the surface finish. However, the stress levels in the diaphragm are very low compared to the breaking strength, so that breakage should not occur. In applications with a high shock loading, additional protection could be provided by mechanically limiting the diaphragm travel.

In the silicon/pyrex model, which has thinner diaphragms, the specific geometry produces a larger deflection [approximately $0.15 \mu\text{m}$ (6 $\mu\text{in.}$) per g]. Also, the calculated stress is larger [8.4 kg/cm^2 (120 psi)]. The corresponding graphs of displacement and stress are shown in Figures 6 and 7.

ACCELEROMETER DIMENSIONS

Based on the above analysis, the diaphragm design has a 0.32 cm (0.125 in.) inner radius and a 0.8 cm (0.312 in.) outer radius. With a 0.48 cm (0.187 in.) wall in the cylindrical frame, the outside diameter is 2.54 cm (1.0 in.), except for the flange area. There the diameter is 3.3 cm (1.3 in.).

The length of the accelerometer is chosen so that the available interior space for the proof mass will be sufficient to achieve the deflections of $0.025 \mu\text{m}$ to $0.15 \mu\text{m}$ (1 to 6 $\mu\text{in.}$). This length is 1.9 cm (0.75 in.). The total length also includes the thickness of the end discs; this was chosen as 0.64 cm (0.25 in.). The overall length of the accelerometer is then 3.18 cm (1.25 in.).

PROOF MASS

The proof mass is dimensioned to occupy approximately 90% of the available interior space. The mass is designed as a circular cylinder, which is clamped to the center post connecting the two diaphragms.

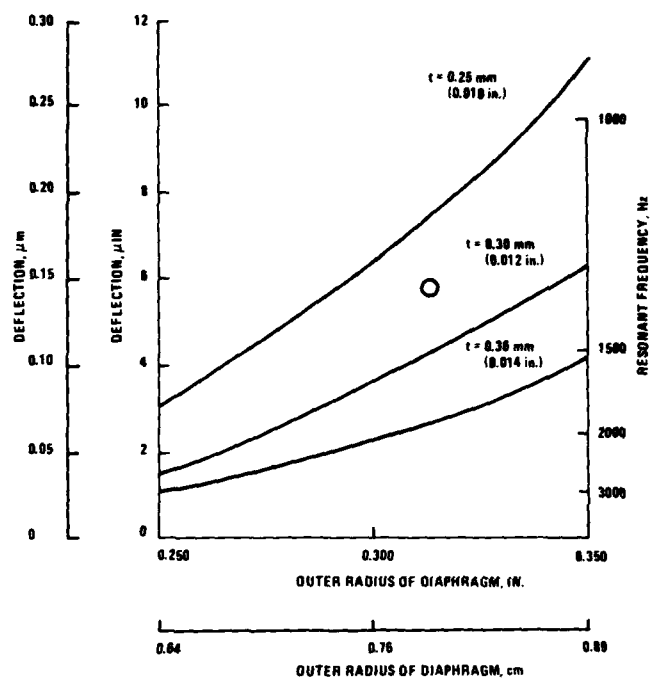


Figure 6. Accelerometer Deflection Per g: Silicon/Pyrex Model

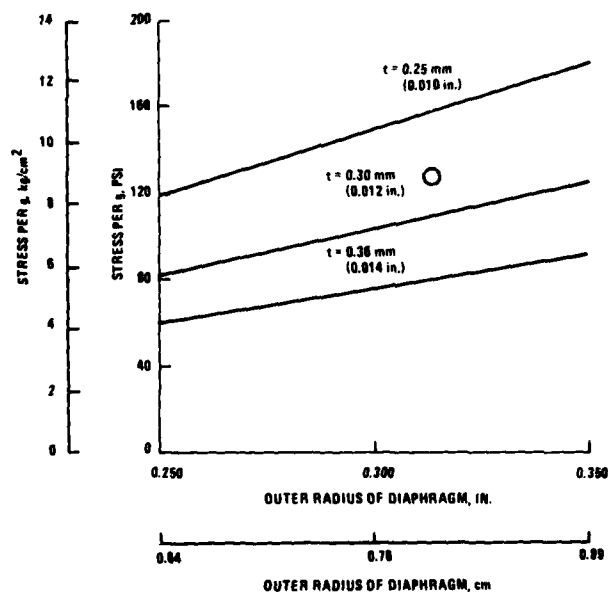


Figure 7. Stress at Inner Radius of Diaphragm: Silicon/Pyrex Model

CAPACITANCE PICKOFF

The capacitance pickoff is designed to take advantage of the spacing modulation due to the deflection, and also to get as large a plate area as practical, so that the effect of stray capacitance is reduced. The center post diameter of 0.64 cm (0.25 in.) is a practical limit on plate size. The plates are made 0.76 cm (0.3 in.) diameter. Plate spacing is chosen for a capacitance near 100 pF, which at the same time provides sufficient spacing for dielectric strength at the applied voltage. A plate separation of 5 μ m (0.0002 in.) is used. This spacing has a voltage breakdown of 300 volts, well above the applied voltage of 10-15 volts.²

MATERIALS SELECTION

At the outset, it was planned to make the diaphragms of single-crystal silicon, as has been described above. The balance of the unit was made either from pyrex or from silicon. The choice was governed by the fabrication and assembly method. It was planned to use the thermoelectric bond for at least part of the assembly. For this bonding method, pyrex was chosen to go with silicon because it is the specific required material for the process, and has a closely matched thermal expansion coefficient. It was on this basis that pyrex was chosen for the end discs for both models, and also for the cylindrical body and post of the pyrex/silicon model where disc diaphragms are used. As is discussed later, when it became clear that thermoelectric bonding was not satisfactory for the pyrex end discs, the optical contact method was used there.

²P. Kisluik, "Arcing at Electrical Contacts on Closure; Part V, The Cathode Mechanism of Extremely Short Arcs," Journal of Applied Physics, Vol. 25, No. 7, July 1954, pp. 897-899.

READOUT ELECTRONICS

The readout electronics are designed with the objective of providing digital readout. To accomplish this, an oscillator configuration was chosen, so that the oscillator frequency will be proportional to the pickoff capacitance, and hence, to acceleration.

The circuit used is shown in Figure 8. The oscillator consists of U_1 and Q_1 with associated passive components while U_2 is a buffer and line driver. The input impedance of U_2 is very high and its effect on the oscillator can be neglected.

Sensor capacitor C_x is alternately charged and discharged with the voltage across C_x compared to V_{ref} , which alternates between two values. The two voltages of V_{ref} are first determined. It is assumed that there is no leakage current through the drain to source of Q_1 and no leakage current through the negative input of U_2 . It is also assumed that the voltage drop across R_3 caused by the charging of C_x is negligible. The high-reference voltage is then

$$V_{refH} = \frac{V_{cc}}{2} \left(1 + \frac{R_{eq}}{R_{eq} + R_3 + R_4} \right) \quad (1)$$

where

$$R_{eq} = \frac{R_5 R_6}{R_5 + R_6} = \frac{R_5}{2}$$

To find the low reference voltage, the fact that $r_d \ll R_3$ is used, where r_d is the drain to source "on" resistance of Q_1 .

V_{refL} then becomes

$$V_{refL} = \frac{V_{cc}}{2} \left(\frac{R_4 + r_d}{R_{eq} + R_4 + r_d} \right) \quad (2)$$

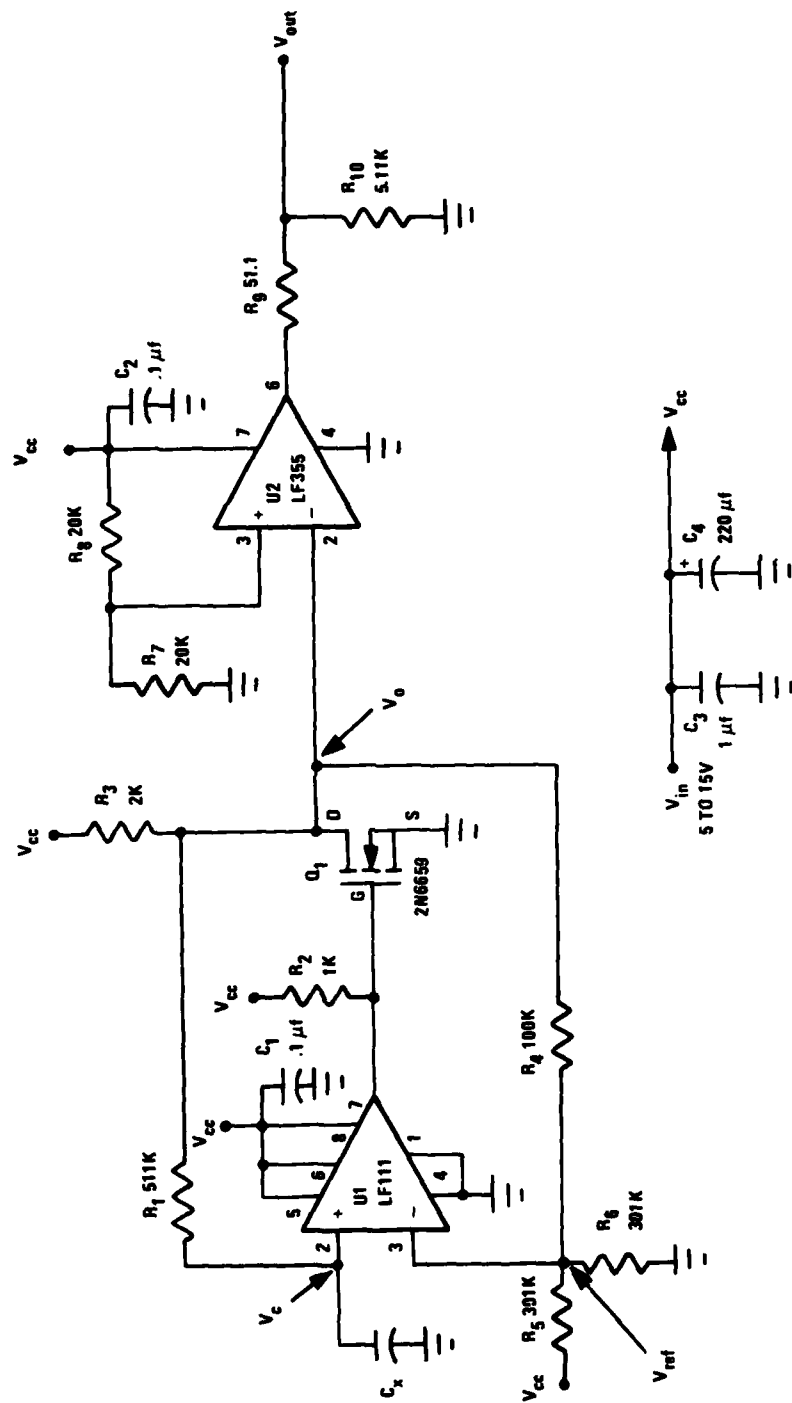


Figure 8. Readout Electronics

but

$$r_d \ll R_4$$

so that

$$V_{\text{refL}} = \frac{V_{\text{cc}}}{2} \left(\frac{R_4}{R_{\text{eq}} + R_4} \right) \quad (3)$$

The hysteresis voltage is defined as the difference between the high and low reference voltages.

$$V_{\text{Hys}} = \frac{V_{\text{cc}}}{2} \left(1 + \frac{R_{\text{eq}}}{R_{\text{eq}} + R_3 + R_4} \right) \quad (4)$$

Substituting values, it is found that

$$V_{\text{refH}} = 0.7980 V_{\text{cc}}$$

$$V_{\text{refL}} = 0.1996 V_{\text{cc}}$$

$$V_{\text{Hys}} = 0.5984 V_{\text{cc}}$$

Voltage across C_x will exponentially oscillate between V_{refL} and V_{refH} (Figure 9). The period of oscillation is $t_1 + t_2$, where

$$t_1 = \tau_1 \ln \left[\frac{V_{\text{cc}} - V_{\text{refL}}}{V_{\text{cc}} - V_{\text{refH}}} \right] \quad (5)$$

$$t_2 = \tau_2 \ln \left[\frac{V_{\text{refH}}}{V_{\text{refL}}} \right] \quad (6)$$

$$\tau_1 = (R_3 + R_1) C_x \quad (7)$$

$$\tau_2 = (R_1 + r_d) C_x \quad (8)$$

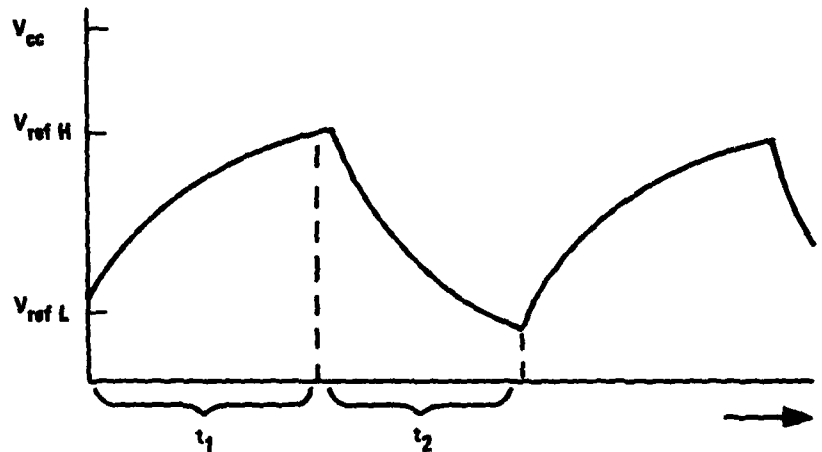


Figure 9. Oscillating Voltage Across C_x

Combining Eq. (1), (2), (5), and (7) gives

$$t_1 = (R_1 + R_3) C_x \ln \left[\frac{(2 R_{eq} + R_4) (R_{eq} + R_3 + R_4)}{(R_3 + R_4) (R_{eq} + R_4)} \right] \quad (9)$$

Combining Eq. (1), (2), (6), and (8) gives

$$t_2 = (R_1 + r_d) C_x \ln \left[\frac{(2 R_{eq} + R_3 + R_4) (R_{eq} + R_4)}{(R_{eq} + R_4) (R_{eq} + R_3 + R_4)} \right] \quad (10)$$

As can be seen from Eq. (9) and (10), the period of oscillation is directly proportional to C_x .

Period is also proportional to $(R_1 + R_3)$ and $(R_1 + r_d)$; however,

$$R_1 \gg R_3 \gg r_d$$

so that the main source of error is R_1 . It is, therefore, very important to choose a very low-temperature coefficient for R_1 . Resistors R_2 through R_6 all appear as arguments of the log function and have a weaker effect on the period. Low-temperature coefficients should be chosen for these resistors, but it is not nearly as critical as for R_1 .

Note that V_{CC} has dropped out of the equations. It was assumed that V_{CC} at the start of a period was equal to V_{CC} at the end of a period. This condition is met with a well-regulated power supply and high-frequency bypass of the power supply lead (C_3 and C_4 of Figure 8).

Throughout this analysis, zero offset voltage at the input to U_1 is assumed. However, an offset voltage does exist. This offset voltage is a function of V_{CC} , temperature, and time. The offset voltage is extremely small, and its effect has been minimized by setting V_{Hys} large. Leakage currents are also extremely small and have been neglected.

As described above, R_1 is the most significant parameter affecting the oscillation frequency. The stability of R_1 was maximized by using low-temperature coefficient resistors. In addition, a batch of resistors was tested to determine the temperature coefficient of each. Then the most stable matched pairs were selected for use in the two oscillators. This helps assure the minimum frequency dependence on temperature. Also, with matched pairs, both oscillators will track together so that the frequency difference, which is the output signal, is further stabilized.

The difference of the oscillator frequencies is obtained in an up-down counter. The counter registers the net frequency difference as pulses per unit time proportional to acceleration.

Each oscillator has a power supply decoupling network, as shown in Figure 8. This is needed to render negligible any common coupling impedance through the power supply. Any coupling between the oscillators will contribute to lock-in when the oscillators are sufficiently close in frequency.

SECTION 4

FABRICATION

Two models of the accelerometer were constructed: both models are similar, but differ in whether the diaphragm is integral with the outer cylindrical frame, or if it is a disc bonded to the frame. These two methods of fabrication were chosen because each has its distinct advantages. The integral diaphragm approach has the advantage of no bonding between the diaphragm and the cylindrical frame; hence, a possible source of instability is removed. In terms of fabrication, this approach is more complex because of the additional machining required to generate the body, diaphragm, and center post. Also, the interior side of the diaphragm does not readily lend itself to polishing. The other approach, using separate silicon discs as diaphragms, has the advantage that the diaphragms can be fabricated from silicon wafers such as those used in the semiconductor industry. Each wafer can readily be polished on both sides and cut to the proper diameter. Fabrication of each model is described below.

INTEGRAL DIAPHRAGM MODEL

This model is made from single-crystal silicon stock in the form of a "cup" containing the diaphragm, center post, and outer cylinder. Two such cups are then joined to each other to make an enclosed, two-diaphragm unit. The outside surface of the diaphragm is polished optically flat; the inner surface is etched to remove grinding stresses. A capacitor electrode is sputter-deposited on the outer polished surface of the diaphragm, along with a connecting tab extending to the outer edge. The end discs, which constitute the capacitor frame, are machined from pyrex and polished optically flat. Pyrex was used because it was planned to bond these discs to the outer rim of the diaphragm, using thermoelectric bonding. It was later

found that this bonding method was not suited to this geometry, because the process also produced unwanted bonding in the capacitor area. Because of this, optical contact bonding is used instead to attach the pyrex end disc to the accelerometer at each end.

The spacing for the capacitor is made by masking and etching the pyrex end disc to a depth of 5 μm (0.0002 in.). The masking preserves an annulus at the outer rim of the disc for the optical contact bond. This annulus is traversed by an etched channel to provide clearance for the electrode tab deposited on the diaphragm. The end disc is drilled to make a 1 mm (0.040 in.) diameter hole. The capacitor electrode is deposited by an electrodeless nickel process, which also provides a plated through path in the hole to a soldering tab on the opposite side.

The proof mass is made of copper because of its non-magnetic properties and simplicity in machining. The proof mass is made in two identical parts, each mass associated with its corresponding half of the cup. This arrangement allows for some slight eccentricity as a result of bonding the two center posts to each other. Each proof mass is clamped to the center post.

Prior to bonding, gold is sputter-deposited on the interface surfaces. Gold diffusion bonding is accomplished by heating to 430°C in an oven purged with nitrogen. The two parts are held in a fixture which assures concentricity in the assembly and also permits loading to 0.42 kg/cm² (6 psi). At the same time, provision is made to rotate (or "scrub") one part with respect to the other at the bonding temperature. After gold diffusion bonding, the pyrex end discs are attached by a direct optical contact method. Figure 10 shows a photograph of the piece parts for this model, and the assembled unit is shown in Figure 11.

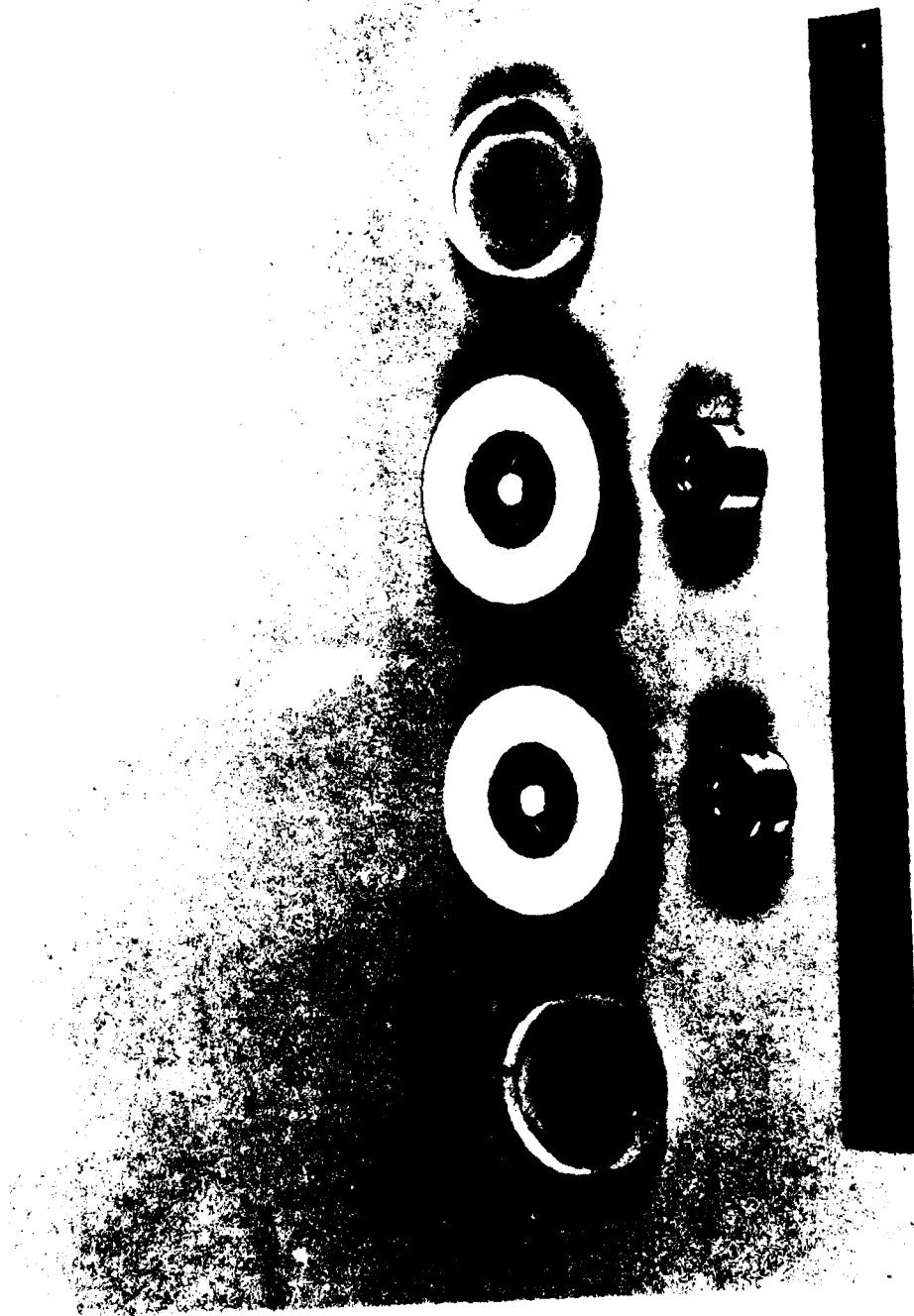


Figure 10. Piece Parts for Integral Diaphragm Model

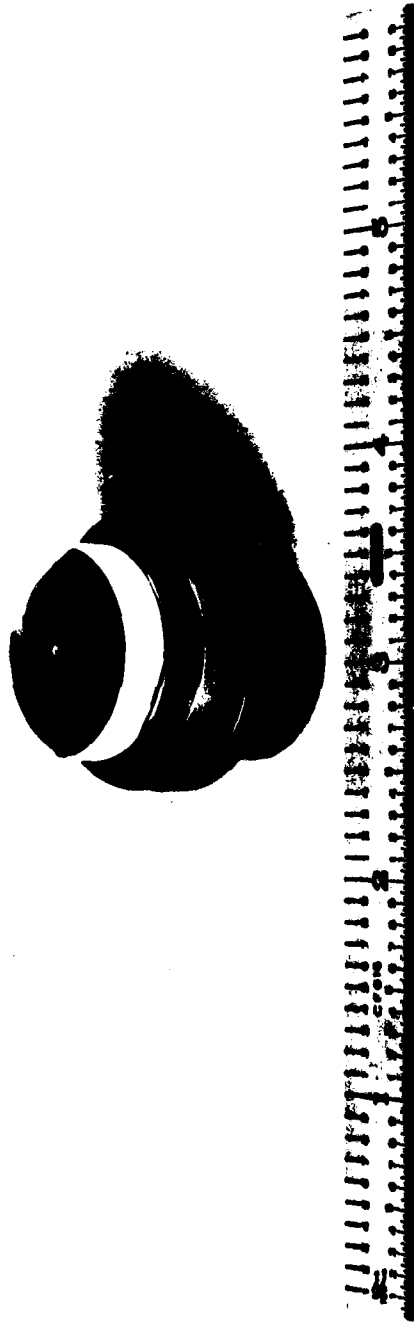


Figure 11. Assembled Integral Diaphragm Accelerometer

SILICON/PYREX MODEL

This model uses a pyrex body and center post, and single-crystal silicon diaphragms. To assure matched parts, the pyrex parts are made from stock polished optically flat on both sides, and of the proper thickness corresponding to the length of the center post and body. Then the post and hollow-cylindrical body are cored from this polished pyrex stock to produce matched parts of equal length. The diaphragms are made from single-crystal silicon polished to 0.4 mm (0.016 in.) thickness. The capacitor electrodes are sputter-deposited on the diaphragm, as in the other model. The pyrex end discs used for the pickoff capacitors are identical to those made for the other model.

The proof mass, made of copper, is clamped to the center post which joins the two diaphragms. One proof mass is used in this model since the center post is one continuous piece for its full length.

In assembling this model, thermoelectric bonding is used to join the pyrex body and the center post to the silicon diaphragms. The process is carried out in a heated oven purged with nitrogen. A voltage is applied across the bond interface, and a diminishing current flow is observed during bonding. Measurement of the current affords a method of monitoring the progress of the bonding process. The thermoelectric process makes a strong bond between silicon and pyrex. A disadvantage is that there is some distortion of the silicon diaphragms in the peripheral bonding region, and the surface is no longer flat. Another limitation of the process shows up in bonding to the pyrex end discs. It was found in tests of bonding diaphragms to the pyrex end discs that the bonding also progresses into the etched recess for the pickoff capacitor. The effect is attributed to the high electrostatic forces present during thermoelectric bonding. Optical contact was considered for attaching the pyrex end discs, but it could not be used because the contact surface on the silicon diaphragm is not sufficiently flat after the thermoelectric bonding. Figure 12 is a photograph of the piece parts for this model.

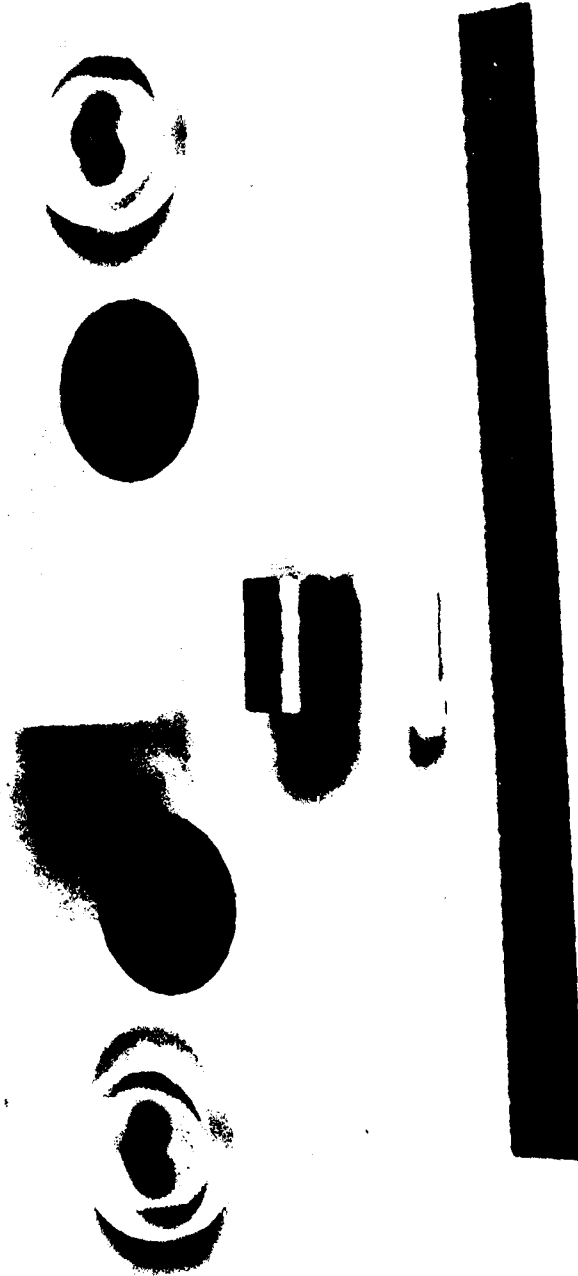


Figure 12. Piece Parts for Silicon/Pyrex Model

ELECTRONICS

The readout electronics, consisting of the oscillator and driver sections, is fabricated on a conventional, universal printed circuit card, sized to accommodate the circuit. The electronics for each pickoff capacitor is built on its own card, so that it can be mounted very close to the accelerometer in the test fixture, in order to reduce the effects of stray capacitance.

SECTION 5

TESTING

Testing was carried out on the integral diaphragm accelerometer in a 1g field. A precision dividing head mounted on a stable granite pier is used for orienting the input axis with respect to the local vertical. The accelerometer is mounted in a test fixture attached to the dividing head, as shown in Figure 13. Also shown are the two readout electronics cards, mounted in close proximity to each end of the accelerometer. This allows the lead from the capacitance pickoff to come directly to the input circuit of the oscillator with minimum lead length. The output from each electronics card is connected to an up-down counter, to produce the differential pulse count proportional to acceleration. The counter is equipped with a time base and printer for data recording. A temperature chamber is fitted to the dividing head, so that the accelerometer temperature can be varied above and below room temperature. The test setup is shown in the photograph in Figure 14.

Tests were conducted to measure scale factor and bias, and their temperature dependence. Scale factor linearity was also measured, and reaction time determined. Scale factor and bias are determined from 0° , 90° , 180° , 270° , and 360° positions of the input axis. Scale factor linearity is determined by varying the position of the input axis in steps of 0.2g over the range of 0 to 360° .

Results of the tests show milli-g fluctuations in bias and scale factor. The possible causes of these variations were examined in considerable detail by interchanging electronics and changing mounting arrangements. It is concluded that the effects arose from mechanical effects within the accelerometer rather than in the electronics. The results of these tests are listed below:

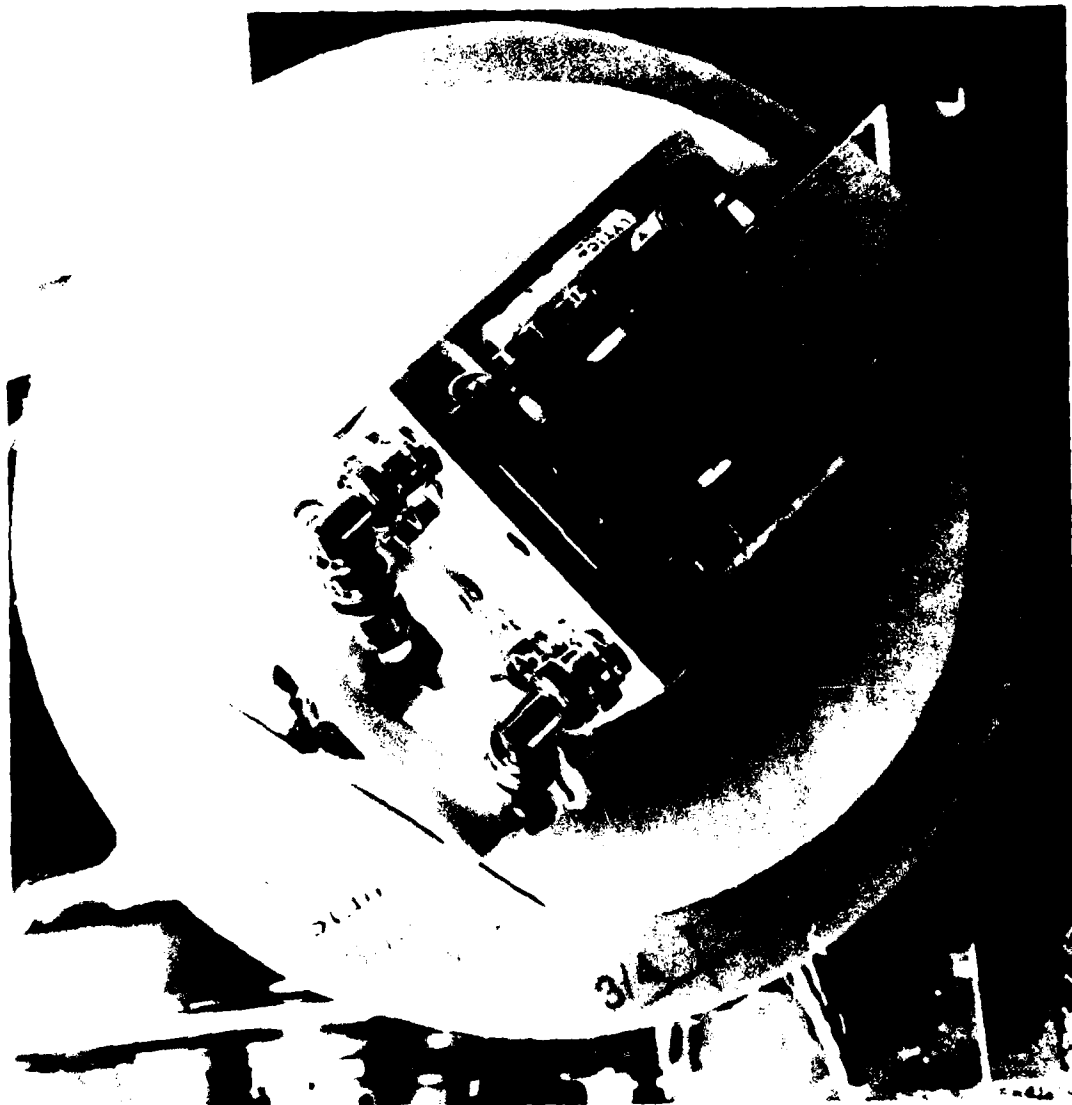


Figure 13. Accelerometer Test Fixture on Dividing Head (Readout electronics and accelerometer in place.)

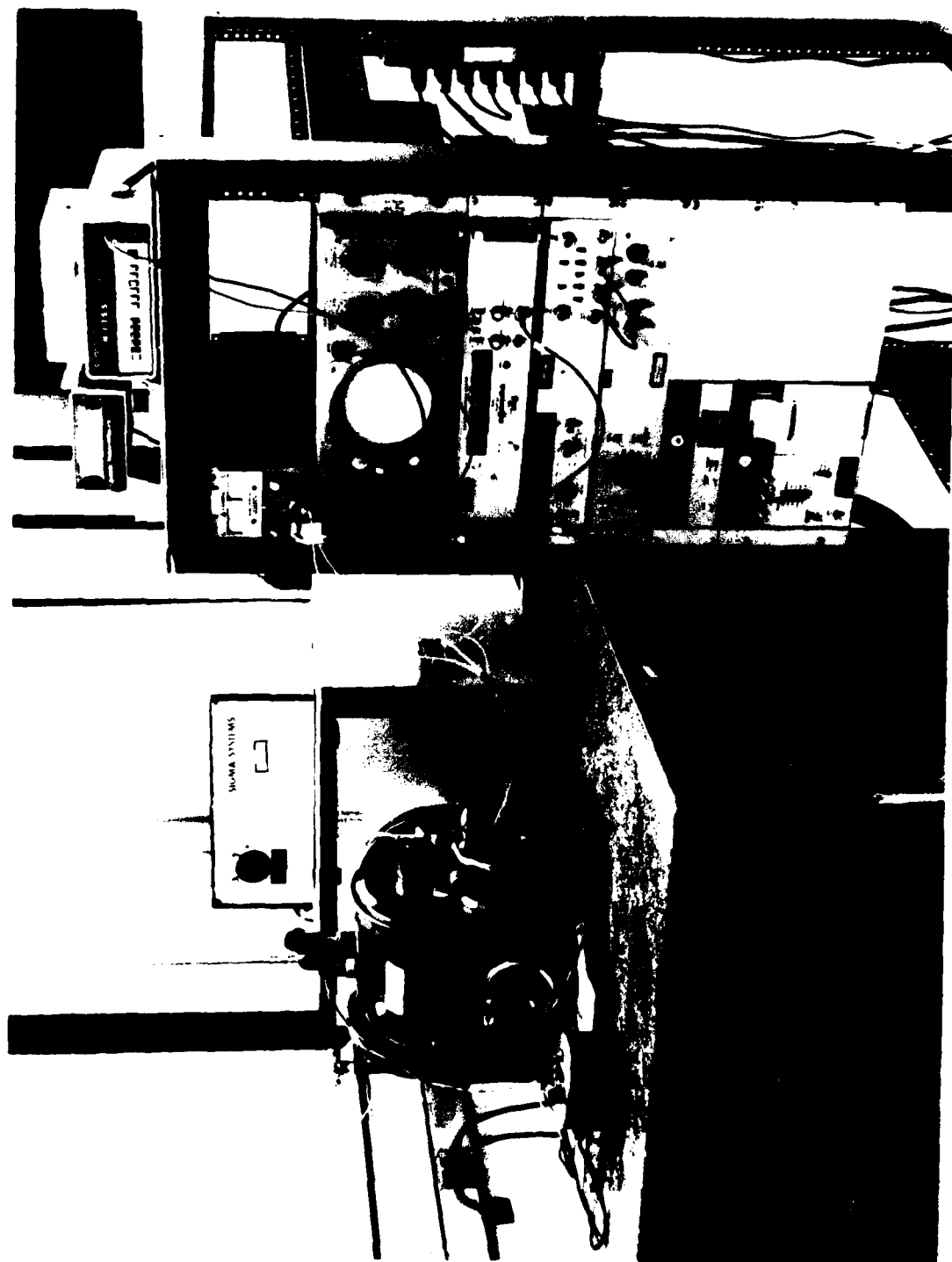


Figure 14. Test Setup Showing Dividing Head, Temperature Chamber, and Data Recording Rack

Bias stability	$11.5 \times 10^{-3} \text{ g}^*$
Bias temperature sensitivity	$1.1 \times 10^{-3} \text{ g/}^\circ\text{C}^\dagger$
Scale factor stability	$1.4 \times 10^{-3} \text{ g}^*$
Scale factor temperature sensitivity	$3.5 \times 10^{-3} \text{ g/}^\circ\text{C}^\dagger$
Scale factor linearity deviation	$1.5 \times 10^{-3} \text{ g RMS}$
Scale factor symmetry	$1.2 \times 10^{-3} \text{ g RMS}$
Threshold	$110 \times 10^{-6} \text{ g}$
Reaction time	3 minutes
Dynamic range	not tested

Fluctuations in the milli-g range are associated with the bias, scale factor, and linearity data. These effects appear to be inherent in the structural characteristics, and are, to a degree, dependent on input axis orientation. This is borne out in the scale factor linearity measurements. The magnitude of the errors clearly indicates the need for a very considerable improvement in stability to make the concept viable for navigation applications. The source of these instabilities is attributed to residual stresses in the diaphragms, resulting from the high-temperature bonding process. The key to improved performance lies in producing stress-free, silicon-to-silicon bonds. Lowering the bonding temperature is one approach to reducing bonding stress. The gold diffusion process is governed by the parameters of temperature, pressure, and time. These parameters can be manipulated to lower bonding temperature.

*The bias and scale factor stability data are obtained from an average of a set of data taken one day, compared to the average of a set of data taken another day.

†The temperature sensitivity data are obtained from the average of a set of data taken at one temperature, compared to the average of a set of data taken at a second temperature.

SECTION 6

RELIABILITY AND MAINTAINABILITY

In considering reliability and maintainability of the monolithic accelerometer, the possible failure modes will be identified and their associated reliability discussed. Eight possible failure modes, discussed below, have been identified. These failure modes are considered for the integral diaphragm model.

GOLD DIFFUSION BOND

One gold diffusion bond is used to join the two silicon cups. The bond interface consists of an annulus formed by the outer rim of one cup and its mounting flange, joined to the corresponding surface of the second silicon cup. Also included is the circular area of the end of the central post inside the cup, joined to the corresponding surface of the second cup. The bonding process involves sputter deposition of gold on the mating surfaces, followed by heating under load to complete the bond.

OPTICAL CONTACT BOND

The outer surface of the diaphragm and one side of the end disc are joined by optical contact. The contact surface on the end disc is an annulus produced as a result of etching the central part of the disc to form the spacing for the pickoff capacitor. The two optically flat surfaces are bonded by placing them in contact under modest loading and observing disappearance of any optical interference pattern (fringes). In the future, the accelerometer configuration will use silicon end discs bonded by a gold diffusion process.

DIAPHRAGM RUPTURE

The diaphragm supporting the proof mass undergoes load-induced stress as acceleration is applied. These stresses are larger at the inner radius than at the outer radius because the loading is distributed along a smaller circumference. The calculated stress at the inner radius ranges from 2.8-5.6 kg/cm² (40-80 psi) per g for the diaphragm geometries, or 28-56 kg/cm² (400-800 psi) for 10g. On the other hand, the modulus of rupture ranges from 700 to 3500 kg/cm² (10,000-50,000 psi) for silicon. For some conditions of shock it may be necessary to limit the travel of the diaphragm with mechanical stops.

MASS ATTACHMENTS

In the accelerometer, the proof mass is clamped to the center post. This mechanical attachment is a possible mode of failure at high-g shock levels. Clamping is by means of circumferential contact to the center rod in the present model. In the future, attachment of the proof mass will be ruggedized either as a shrink or interference fit, or the geometry will be rescaled so that the proof mass can be of the same silicon material as an integral part of the accelerometer.

CAPACITOR ELECTRODE ON END DISC

The end disc of the accelerometer has an electrodeless, nickel-plated capacitor surface. The plating arrangement carries electrical continuity through a hole to the opposite side to form a soldering tab. No failure in the adhesion of the plating is expected, so this item does not degrade the reliability.

CAPACITOR ELECTRODE ON SILICON DIAPHRAGM

The capacitor electrode on the silicon diaphragm is sputter-deposited. No failure in the adhesion of the deposited electrode is expected, so this item does not degrade the reliability.

WIRING CONNECTIONS TO CAPACITOR ELECTRODES

In the present model, the connection to the end disc electrode is soldered. The connection to the diaphragm electrode is made by means of a conductive epoxy. In the future, the connection to the diaphragm electrode will also be soldered.

VOLTAGE BREAKDOWN ACROSS CAPACITOR

In the present system, the capacitor plate spacing is 5 μm . The voltage appearing across the capacitor is a sawtooth waveform of frequency 7 and 35 kHz. The voltage amplitude swings between +12 and 0 volts. The voltage breakdown in air tends to remain relatively constant over the separation distance of 1-10 μm , where the minimum sparking potential is 300 volts. In the present system, the applied voltage is well below breakdown potential.

In future applications, consideration must be given to operation at high altitude with reduced pressure. Under reduced pressure conditions, it may be necessary to operate as a hermetically-sealed unit which is pressurized to normal atmospheric pressure. This is in keeping with enclosing the accelerometer in a case to protect it from dust and dirt, as well as providing a mounting arrangement with screw holes.

FAILURE ESTIMATION

Since no established failure rates exist for this new accelerometer concept, a quantitative failure rate can only be achieved by estimation analysis. Various approaches could be taken. For example, an estimated value could be assigned to each of the previously discussed failure modes. Summing these with any discrete piece parts required would provide a value for the overall sensor. This total, of course, can be no more precise than the accuracy of the individual components.

A second approach might be comparison of this design concept to other accelerometers which do have experience-based failure rates. Application of a relative design complexity factor to these known rates would allow prediction of an expected rate for this new design.

A third approach would be comparison to other devices or components which have a generic functional or material similarity. Two examples might be air core capacitors and quartz crystals.

A final consideration is whether an allowance for the necessary associated electronics should be included in the prediction.

Since this development program is centered primarily on evaluation of the acceleration sensing concept itself, and since the auxiliary electronics functions can be accomplished in various ways, they are not included in the summation.

There appears to be no accuracy advantage to any of the three analysis methods discussed previously. Therefore, the most cost-effective approach is chosen: a combination of the second and third methods.

A survey of reliability information published in Mil-Handbook 217, Rome Air Development Center RADC-TR-22, and Honeywell's own accelerometer product line experience developed the following data:

<u>Device</u>	<u>Failure Rate</u> <u>(failures per million hours)</u>
Air core capacitors-- quartz crystals	0.1 to 0.2
Accelerometers-- (general and linear)	2.0 to 50

The above data is for ground use; aircraft applications will be about five times higher.

No wearout modes are anticipated for this device. Its design can be tailored to avoid resonance conditions for a specific application. Therefore, the above failure rates are constant with time and comprised of random-type failures.

In view of this sensor's relative design simplicity, minimal parts count, and use of only a few differing material types, it has inherently high reliability. Since it lacks comparable production experience it is, however, expected to have a higher failure rate initially than a capacitor or a crystal. Therefore, it is estimated that a failure rate in the region of 0.5 to 2.0 failures per million hours can be expected from the sensor. Packaging the sensor with appropriate electronics to provide signal processing for a more typical accelerometer readout will, of course, increase this failure rate somewhat--most probably near the lower end of the range given for accelerometers in the table above.

Because of the device's structural assembly requirements and its simplicity, no field maintainability procedures are envisioned. The same situation is expected for a sensor-electronics package. Therefore, a maintainability analysis and procedure are not required.

SECTION 7

RECOMMENDATIONS FOR FUTURE WORK

Performance improvements in the monolithic accelerometer are linked to ways of reducing residual diaphragm stresses through further simplification of the geometry, reduced bonding temperature, and temperature compensation. Ways of achieving better performance in future work are described below.

LOW-TEMPERATURE BONDING

In considering the best choice of bonding, the results show that the gold diffusion bond is preferred to thermoelectric and optical contact methods. The thermoelectric bonding is not well-suited because of the stresses it induces at the bonding interface. This is particularly true for diaphragm bonding, which should be stress-free. Although the optical contact method has the advantage of low-temperature bonding, it does not have as high a bond strength as the gold diffusion bond. For these reasons, the gold diffusion bond is recommended for all interfaces. Further work is needed to define the lowest useful bonding temperature. The bond strength is a function of pressure, temperature, and bonding time. These parameters can be varied to achieve a lower bonding temperature.

ALL-SILICON END DISCS

In this program, the frame end discs were made of pyrex because it was planned to use thermoelectric bonding to join them to the silicon diaphragm. In terms of attaining maximum stability, it is more desirable to have the same material, silicon, throughout the accelerometer. Therefore, it is recommended that the end discs also be made of silicon.

SINGLE-DIAPHRAGM SUSPENSION

In keeping with using the same material throughout, and also simplifying the parts and number of bonds, a single-diaphragm suspension is attractive. The concept is shown in Figure 15. The accelerometer consists of only three pieces: two end discs and the body. The body is machined and etched from one piece of single-crystal silicon. The proof mass is made an integral part of the diaphragm, and the diaphragm outer edge is integral with the cylindrical body. To achieve deflection characteristics comparable to using a separate proof mass, the diaphragm is made considerably thinner--0.10 to 0.13 mm (0.004 to 0.005 in.) thick. Under these conditions, the stress level in the diaphragm is still low and comparable to the present system. Since no attachment methods are needed for the proof mass, any attendant stress effects from this source are removed. The number of bonds is also reduced to just two. The readout method is the same as before, using a capacitance pickoff.

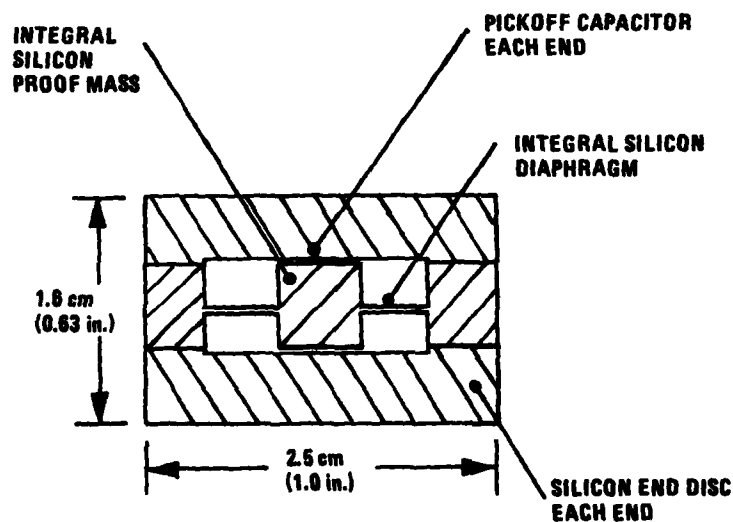


Figure 15. Single-Diaphragm Accelerometer (Only three parts and two bonds are required.)

TEMPERATURE COMPENSATION

Although no temperature compensation was carried out in the present study, it is necessary for improved performance. A basic limitation of temperature dependence arises from the change in Young's Modulus with temperature. The stiffness of the suspension, and hence the scale factor, will be temperature-dependent. Typical values of $\Delta E/E$ are $50 \times 10^{-6}/^{\circ}\text{C}$.³ Therefore, temperature compensation with one or more sensors is recommended.

³H.J. McSkimin, "Measurement of Elastic Constants at Low Temperatures by Means of Ultrasonic Waves--Data for Silicon and Germanium Single Crystals and for Fused Silica," Journal of Applied Physics, Vol. 24, No. 8, August 1953, p. 995.

SECTION 8

CONCLUSIONS

Analysis, design, and testing have been carried out for the monolithic accelerometer having single-crystal silicon diaphragm suspension. The results show milli-g variations in bias, scale factor, and scale factor linearity. This non-rebalance approach, without temperature compensation, requires considerable improvement to make the concept viable for navigation applications.

Further work is required to reduce the bonding temperature and, hence, induced stress. A simplified geometry has also been recommended to reduce the parts count to three and the bonds to just two. Although temperature compensation was deferred in this study, it is recommended in future work.

REFERENCES

1. Roark, R.J., Formulas for Stress and Strain, Second Edition. New York: McGraw-Hill, 1943, Chapter 10.
2. Kisluik, P., "Arcing at Electrical Contacts on Closure; Part V, The Cathode Mechanism of Extremely Short Arcs," Journal of Applied Physics, Vol. 25, No. 7, July 1954, pp 897-899.
3. McSkimin, H.J., "Measurement of Elastic Constants at Low Temperatures by Means of Ultrasonic Waves--Data for Silicon and Germanium Single Crystals and for Fused Silica," Journal of Applied Physics, Vol. 24, No. 8, August 1953, p. 995.